Published in final edited form as:
Int J Hyperthermia. 2011 ; 27(8): 782–790. doi:10.3109/02656736.2011.614671.

MR Temperature Imaging of Nanoshell Mediated Laser Ablation

R. Jason Stafford[1], **Anil Shetty**[2], **Andrew M. Elliott**[1], **Jon A. Schwartz**[3], **Glenn P. Goodrich**[3], and **John .D. Hazle**[1]

[1]Department of Imaging Physics, The University of Texas MD Anderson Cancer Center, Houston, Texas U.S.A.

[2]Visualase, Inc., Houston, Texas U.S.A.

[3]Nanospectra Biosciences, Inc., Houston, Texas U.S.A.

Abstract

Minimally invasive thermal therapy using high-power diode lasers is an active area of clinical research. Gold nanoshells (AuNS) can be tuned to absorb light in the range used for laser ablation and may facilitate more conformal tumor heating and sparing of normal tissue via enhanced tumor specific heating. This concept was investigated in a xenograft model of prostate cancer (PC-3) using MR temperature imaging (MRTI) in a 1.5T scanner to characterize the spatiotemporal temperature distribution resulting from nanoparticle mediated heating . Tumors with and without intravenously injected AuNS were exposed to an external laser tuned to 808 nm for 180 sec at 4W/cm^2 under real-time monitoring with proton resonance frequency shift based MRTI. Microscopy indicated that these nanoparticles (140–150 nm) accumulated passively in the tumor and remained close to the tumor microvasculature. MRTI measured a statistically significant (p<0.001) increase in maximum temperature in the tumor cortex (mean=21±7°C) in +AuNS tumors versus control tumors. Analysis of the temperature maps helped demonstrate that the overall distribution of temperature within +AuNS tumors was demonstrably higher versus control, and resulted in damage visible on histopathology. This research demonstrates that passive uptake of intravenously injected AuNS in PC-3 xenografts converts the tumor vasculature into a potent heating source for nanoparticle mediated ablation at power levels which do not generate significant damage in normal tissue. When used in conjunction with MRTI, this has implications for development and validation of more conformal delivery of therapy for interstitial laser ablations.

INTRODUCTION

Thermal ablation of tumors has undergone rapid evolution over the last decade as it has grown into a more widely accepted minimally invasive alternative to some conventional surgical interventions, particularly in cases where the patient is not a suitable surgical candidate or disease has been detected early and is well localized [1–9]. These *in situ* approaches to focal treatment of lesions often require only minimal anesthesia and are associated with a reduction in normal tissue morbidity and complications, thereby potentially reducing the impact of the therapeutic intervention on the patient as well as overall cost. Thus, the minimally invasive nature and non-ionizing radiation associated with thermal therapies translates into low impact, repeatable procedures ideally suited for non-surgical candidates or palliative management, but is increasingly being investigated in the management of early detected local disease.

CORRESPONDING AUTHOR R. Jason Stafford, Ph.D. 1400 Pressler Street, Unit 1472 Houston, TX 77030 Phone: 713-563-5082 jstafford@mdanderson.org.

Percutaneous approaches to ablation include cryotherapy [10], radiofrequency [11], microwave [12], high-intensity ultrasound [13, 14] and laser [15]. In particular, interstitial laser ablation systems featuring small, compact, high-power solid state lasers, cooled applicators for generation of larger lesions, and integrated workstations for MR temperature imaging guidance, are now commercially available. MR-guidance plays a facilitating role in expanding the use of rapid thermal ablation using high power lasers via the integration of real-time MR temperature imaging (MRTI) feedback during therapy [16, 17], which can be used to help estimate both the extent of tissue damage for efficacy as well as to help enforce temperature limits in nearby critical structures and near the laser fiber to prevent charring to minimize complications and enhance the safety of these procedures [18–20]. Therefore, in addition to providing superlative soft-tissue contrast mechanisms for planning, targeting and verifying therapy delivery, MRTI adds the ability to effectively monitor delivery of energy in the tissue and therefore opens the door for incorporation of feedback loop based control.

An increasing number of optically activated metal-based nanoparticles are being investigated for therapeutic uses which have the property that the conduction band electrons exhibit a plasmon resonance which greatly increases absorption near the resonance wavelength [21, 22]. These particles can be constructed in a manner to “tune” this absorption wavelength to occur in the near infrared (NIR) part of the spectrum, which currently is the wavelength used by lasers for interstitial ablation [23, 24]. Nanoparticle enhanced absorption results in substantial heating at an applied power well below that needed for laser ablation of tissue, providing a mechanism for targeted tumor heating and sub-lethal heating of adjoining normal tissue. Additionally, although their distribution is not homogeneous throughout the tumor, these tiny particles also accumulate preferentially in tumor tissue passively via enhanced permeability and retention (EPR) or by functionalizing the surface chemistry to bind to specific moieties [25]. This mechanism makes the tumor vasculature a heat source [26] and opens the possibility for providing a much more conformal delivery of heat to the tumor tissue during interstitial laser thermal therapies.

In this work, we used MRTI to investigate the use of gold-silica nanoshells (AuNS), which exhibit a tunable plasmon resonance determined by the thickness of the gold shell surrounding the silica core [21], for AuNS mediated thermal ablation. For the purposes of demonstrating uptake and tumor specific heating, the resulting spatiotemporal temperature distributions during laser irradiation in prostate tumor xenografts associated histology and microscopic distribution of particles in the tumor tissue post intravenous infusion of AuNS in mice were analyzed.

MATERIALS & METHODS

Nanoparticle Fabrication & Preparation

AuNS fabrication followed the method of Oldenberg et al [27]. Gold colloids 1–3 nm in diameter were grown over an aminated, 120 nm (± 12 nm) core of colloidal silica (Precision Colloids, LLC, Cartersville, GA) using the method of Duff and Baiker [28]. Finished particles possessed a 12- to 15-nm-thick shell that yielded an optical absorption peak between 780 and 800 nm. Thiolated polyethylene glycol (5000 MW SH-PEG; Laysan Bio, Huntsville, AL) was then assembled on the AuNS (AuroShell® particles; Nanospectra Biosciences Inc., Houston, TX) surfaces by combining 5 μM SH-PEG and AuNS in deionized H_2O for 12 h at a ratio of 1.5 μl/ml followed by diafiltration to remove the excess SH-PEG. PEGylation was used to keep particles from aggregating in solution as to increase circulation time [29]. Particles were then suspended in 10% trehalose solution to create an iso-osmotic solution for injection at an extinction of 100 ± 5 optical density (OD) units confirmed by spectrophotometry at 800 nm of a diluted sample.

MRTI of Nanoparticle Mediated Heating in PC-3 Xenografts

All animal studies were performed in accordance with the Institutional Animal Care and Use Committee of the University of Texas M. D. Anderson Cancer Center. A human prostate cancer cell line (PC-3; ATCC, Manassas, VA) was cultured and the harvested cells were embedded in a growth promoting substrate (Matrigel, BD Biosciences, San Jose, CA) prior to subcutaneous inoculation (0.2 ml; 5×10^6 cells) on the backs of 4–6 week old immune compromised CB17-Prkd c SCID/J mice. Tumors were grown to a tumor burden of <1 cm maximal diameter. A tail vein injection of the PEGylated AuNSs (9 μl/g by mouse weight) was administered 24 hours prior to laser illumination. A depilatory agent was applied to the region to expose the skin surface and swabbed with PEG diacrylate (Aldrich) for better optical coupling and penetration. Tumors were illuminated with an external continuous wave 808 nm diode laser source (Diomed 15 Plus EVLT; Sigmacon Medical Products, Ontario, Canada) at 4 W/cm^2 for 3 min under real-time MRTI monitoring (Figure 1).

All imaging was performed on a 1.5 T clinical MR scanner (Excite HD, GE Healthcare Technologies, Waukesha, WI) equipped with high performance gradients (40 mT/m maximum amplitude and 150 T/m/s maximum slew rate) and fast receiver hardware (maximum receiver bandwidth ± 500 MHz). A 3” spiral radiofrequency surface coil (courtesy of R. Giaquinto, General Electric Corporate Research and Development, Schenectady, NY), optimized for small animal imaging in the 1.5T environment, was used for signal reception. MR temperature imaging utilized the temperature sensitivity of the water proton resonance frequency shift [30, 31] calculated via a complex-phase difference method as measured from a radiofrequency spoiled gradient-recalled acquisition [32, 33]. Acquisition used a 4 cm × 2 cm field of view with an acquisition voxel size of 0.16 mm × 0.16 mm × 2 mm at 5 s per image (TR/TE/FA = 74 ms/10 ms/30°, receiver bandwidth =70 Hz/pixel).

All data processing reported here was performed off line and implemented on software written in-house (MATLAB, Mathworks, Nattick, MA). Temperature changes were estimated from the complex phase-difference MRTI using a temperature sensitivity of −0.0097 ppm/°C, the field strength and the sequence echo-time (TE) [34, 35]. An SNR threshold was applied to remove random phase that would be generated in regions of low signal (i.e., skin, air, etc) and images were denoised using a 3×3 pixel spatial Wiener filter.

Histology & Microscopy

Animals were euthanized and sent for necropsy 16 hrs post-therapy. Each tumor was divided into two sections as congruent to the acquired MRTI plane as possible. One section was snap-frozen and the other section was fixed in 10% buffered formalin for 3 days and then sectioned for hematoxylin and eosin (H&E) staining to evaluate the extent of necrosis. Digital images were captured and the necrotic border was outlined by an experienced pathologist.

Some sections were stained with silver to emphasize the gold on fluorescence microscopy. A 5 μm thick paraffin section was de-waxed and hydrated to water prior application of silver treatment (HQ Silver Enhancement Kit; Nanoprobes, Yaphank, New York) for 20 min. Sections were washed with water, dried, and pre-mounted with cover slips. Samples were examined using a fluorescence microscope equipped with a polarizing filter (ImmunoGold Silver Staining filter; Nikon Inc., Mellville, New York).

Scanning electron microscopy (SEM) images were acquired to visualize the distribution of AuNS in relation to the tumor vasculature. Thirty-micron sections from the paraffin embedded tissue blocks were cut in a cryostat, mounted on a glass slide, and air dried for 20 min. Samples were then fixed with 4 % paraformaldehyde in PBS for 30 min and sections

rinsed with distilled water and dehydrated in an increasing series of ethanol (50, 70, 80, 90, 100, 100% ethanol, 5 min at each step). The samples were infiltrated with an increasing gradient of HMDS (hexamethyldisilaxane) in ethanol (2:1, 1:1, 1: 2 and 3 changes in pure HMDS, 5 min each time) and dried overnight in a chemical fume hood overnight. The samples were then carbon coated under vacuum using an evaporator (Balzer MED 010). Sections were examined in an SEM (JSM-5900, JEOL USA, Inc.,Peabody,MA) at an accelerating voltage of 15kV.

Transmission electron microscope (TEM) images were acquired to examine the shape of the AuNS and to visualize their location at the cellular level. Samples from the paraffin fixed tissue block (~1mm^3 cubes) were fixed with a solution containing 3% glutaraldehyde plus 2% paraformaldehyde in 0.1 M cacodylate buffer, pH 7.3, for 1 hour. After fixation, the samples were washed and treated with 0.1% Millipore-filtered cacodylate buffered tannic acid, postfixed with 1% buffered osmium tetroxide for 1 hour, and stained en bloc with 1% millipore-filtered uranyl-acetate. Samples were dehydrated in increasing concentrations of ethanol, infiltrated, and embedded in Spurr's low viscosity medium. The samples were polymerized in a oven (70°C for 2 days) then ultra-thin sections were cut in a Leica Ultracut microtome (Leica, Deerfield, IL), stained with uranyl acetate and lead citrate in a Leica EM Stainer, and examined in a TEM (JEM 1010, JEOL, USA, Inc., Peabody, MA) at an accelerating voltage of 80 kV. Digital images were obtained using AMT Imaging System (Advanced Microscopy Techniques Corp, Danvers, MA).

Nuclear Activation Analysis (NAA) of AuNS Uptake

Nuclear activation analysis of gold content was performed in order to assess the uptake of AuNS in the tumor as performed previously by James, et al [36]. NAA uses neutron capture to excite stable gold ($^{79}Au^{197}$) to radioactive gold ($^{79}Au^{198}$) which decays with a half-life of 2.7 days, emitting characteristic 412 keV gamma rays which are used to quantify gold content. Tumor (n=5), liver and spleen (n=1) tissue was excised from untreated mice 16 hours after receiving AuNS dose in order to provide a check against previous results. The tissue was prepared and sent to the Nuclear Engineering Teaching Laboratory at the University of Texas at Austin for NAA analysis which returned the amount of gold per unit weight of tissue (μg/g).

RESULTS

MRTI of Nanoparticle Mediated Heating in PC-3 Xenografts

Tumors were oblong, with an average tumor size was 5.8 mm ± 0.9 mm (4.4 mm – 7.4 mm) in maximal diameter and 3.2 mm ± 0.9 mm (1.5 mm –4.9 mm) in depth as measured via T2-W MRI. Control tumors received laser irradiation but no AuNS. Average maximal temperature change occurring just distal to the skin surface was 19.2°C ± 2.7°C (n=7) with a range of 15.7°C–23.5°C. For +AuNS tumors, the average maximal temperature change was 40.9°C + 2.6°C (n=7) with a range of 38.3°C – 45.0°C. The difference between these means was 21.7°C ± 3.5°C (p<0.001), where significance was assess using a one-tailed Student's T-test. Figure 2 shows a typical example of the differences observed between the MRTI in control versus AuNS injected mice Additionally, histograms of the maximal change in temperature within the tumors of a single control and single AuNS mouse further illustrate that there is a significant shift in the heating distribution throughout much of the tumor (Figure 3.a). The +AuNS tumors also heated faster and maintained increased temperatures deeper into the tumor than control subjects (Figure 3.b–c). Non-linear least squares fitting of the parameters (β_1, β_2) of an approximation of an analytical solution to the heat equation assuming the maximum change in temperature occurs at shallow depth with negligible perfusion [38] was fit using the MRTI data according to the equation:

$$\Delta T = \begin{cases} \frac{\beta_1}{\beta_2} \ln 1 + \beta_2 \cdot \tau & \tau \leq \tau_f \\ \frac{\beta_1}{\beta_2} \ln \left(1 + \frac{\beta_2 \cdot \tau_f}{1 + \beta_2 \cdot \tau - \tau_f}\right) & \tau > \tau_f \end{cases}$$

Where τ is the time passed since the laser exposure started and τ_f is the time the laser exposure was terminated. Excellent agreement was observed (Figure 3.b). Using the registered T2-W images, the spatial profile of temperature over time demonstrated heating in the cortex of the tumors (Figure 3.c). Across all +AuNS subjects, the ΔT_{max}=23°C isotherm extended 2.8 mm ± 0.7 mm into the tissue while the 17°C isotherm extended 3.9 mm ± 0.6 mm. For a subject at a body temperature of 37°C, this would correspond to the 60°C and 54°C isotherms respectively.

Histology & Microscopy

Although temperatures are sufficient to heat the tissue and cause thermal necrosis at depth (Figure 2.b), characterized by a mixed hypereosiniphilic and hyperchromatic region on the H&E stain (Figure 2.c), the highest prolonged temperatures occured primarily in the upper part of the tumor where the tissue seemed to preserve its architectural and cytological detail ("thermal fixation") [37]. Upon higher zoom (not shown), the appearance of thermal damage on the H&E stains included the expected range of cellular degeneration (cellular swelling, hyperchromatic cytoplasm, condensed nucleus, pychnotic nucleus, cellular debris) and coagulative necrosis characteristic of ablative temperatures which are expected with these treatments. The differences in the depth of necrosis measured by H&E staining at 24 hours post-therapy was statistically significant ($p<0.01$), with a mean of 0.1 (0.0,0.4) mm for the control and mean of 2.7 (1.5, 6.1) mm for the +AuNS treated group.

On silver stained sections, the silver coating of the AuNS markedly enhanced the diameter of the particles and causes them to appear bright when polarized UV light hits the silver enhanced particles. Individual particles could be distinguished in regions where there were not many particles. These sections demonstrated that the AuNS accumulated near the tumor blood vessels via passive extravasation (Figure 4.b). Some elastic fibers also fluoresced, but could be distinguished from the AuNS via morphological discrimination, since AuNS appeared elliptic bright objects while elastic fibers presented as streaky wisps of blue. These micrographs and fluorescent microscopy demonstrated the gross distribution of AuNS in the tumors.

Very high magnification (100,000×) TEM images (not shown) of AuNS were used to measure the apparent diameters of the AuNS which was approximately 150 nm. At 30,000×, TEM images showed the relative size of these AuNS versus cellular components (Figure 4.a). AuNS appeared circular in shape, brighter at their edges than at the center, and measured approximately 140 nm in diameter on 25,000× magnification SEM images (not shown). SEM imaging which zoomed into specific vessels corroborated previous reports, as well as silver stain observations which implied that AuNS tended to be prevalent near the tumor vasculature and in these instances appeared to be distributed perivascularly. In these images, the AuNS generally appeared be at distances <15 μm from the vessel wall for these tumors (Figure 4.c & d).

Nuclear activation analysis of uptake

Nuclear activation analysis of the gold content in tumor tissue (n=5; completely untreated tumors) measured a mean of 11.2 ± 2.7 (range: 7.8–13.9) micrograms of gold per gram of tissue (μgAu/g). Liver and spleen levels of gold were tested for one mouse, giving 137.9 and 1874.7 μgAu/g respectively. For this animal, 199 μl were injected corresponding to 447 μg

of gold. This corresponds to a %ID/g of 31, 419 and 3 for the liver, spleen and that animal's tumor respectively.

DISCUSSION

A study demonstrating effectiveness of AuNS therapy in a large animal or in humans has not been performed. While this work is not meant to address this deficit, it is meant to look more closely at the spatiotemporal heating generated during AuNS heating in a model often used to show tumor response to this therapy using AuNS which have already been demonstrated to be non-toxic and are already in clinical trials in humans.

Here, tumor uptake and heating of intravenously injected AuNS in a PC-3 xenograft model has been demonstrated. MRTI of AuNS mediated thermal therapy was used to depict the spatiotemporal temperature history during the laser exposure illustrating the rates of heating and penetration of the laser into the tumor. This feedback in experimental tumor models can be used to develop and validate approaches to therapy as well as numerical simulation. Given that heating depths were not consistent or predictable with a given laser exposure, it is likely that MRTI can play an important role in the monitoring and control of these therapies to aid in the efficacy and safety of delivery as they translate into the clinic.

Imaging the smaller tumors with a clinical MR system was challenging. However, the use of a lower, clinical field strength MRI aided in mitigating susceptibility errors from both equipment and air-tissue interfaces during imaging. Since the primary goal was to directly observe the difference in heating via MRTI, tumor selection was accomplished by using the largest tumor available for treatment, but not over the 1 cm diameter burden imposed by the IACUC. The primary reasons for exclusion included data acquisition failures via human error (i.e., wrong exposure time, laser power, etc.) or animal related (i.e., motion during therapy, scab development above the treatment zone, intramuscular lesion growth, etc). Because the failure rate was not known ahead of time, and these losses were our primary uncertainty, these experiments were approached as a pilot study and accrual terminated when enough successful measurements were made to report. Interestingly, of the subjects excluded due to experimental error, one subject was excluded due to receiving 1.5× the dose of AuNS received by other subjects in the study. Incidentally, the maximum temperature measured in this animal by MRTI was 1.4× the average temperature measured in the rest of the subjects, indicating that, for this study and tumor model, we are still operating in a region where increased injection concentration may result in an increased concentration in tissue which results in a proportional increase in response. This corroborates observations demonstrated by phantom studies [39].

While use of a xenograft model exposed via an external laser source is limited for realistic modeling of AuNS mediated ablation, the approach used here gives valuable insights into the design of therapies for *in vivo* applications. MRTI and pathology both indicated that, despite the small tumor diameters used, penetration of high temperatures and thermal coagulation deep into the tumor was somewhat limited and variable for these exposures. While it is noted that the subcutaneous tumors start at a much lower temperature prior to irradiation, this is still important in that it indicates that it is possible that xenograft studies in which tumor regression is used as an endpoint, as opposed to pathological assessment of damage, may be reporting responses based on partial treatments of these small tumors. This was illustrated in a prior study, similar to the current study, in which investigators followed regression of the PC-3 xenografts and still found residual tumor 21 days after therapy [40], which is well past the 24–72 hour window in which cell death from coagulative necrosis would be expected. Thus, regardless of tumor shrinkage, the interpretation and translation of partial tumor ablations into a clinical scenario is difficult to assess, as the goal is often

complete tumor coverage with respect to thermal ablation. The results observed here indicate that placement of the laser fiber interstitially within the tumor may result in translating the source of heating to the tumor vasculature. This could be useful in interstitial approaches to laser ablation where placement of the fiber within the tumor is sub-optimal for complete tumor coverage as well as potentially helping to better confine heating in irregularly shaped lesions. This hypothesis is currently being explored in larger, orthotopically placed, lesions.

Prior observations in PC-3 and other xenograft models using gadolinium based blood pool contrast agents [41] indicate that the peripheral cortex is more permeable than the tumor core which indicates that passive accumulation of the nanoshells is likely to be higher in these areas. This is in line with our observations on microscopy as well as spatial temperature profiles measured by MRTI. The limited penetration implies that when laser energy is impingent from outside the tumor, penetration through the AuNS laden cortex can possibly limit the extent of heating into the core of the tumor unless higher power or longer exposure times are used. However, this study was limited by tumor size and our fixed exposure time with respect to investigating how deep therapy can penetrate into tumor tissue when the laser is placed outside or adjacent. Such an investigation would be better served using a larger tumor and animal model [24] in which the heating distribution within tumors from within and without might be observed by MRTI feedback and compared more effectively for designing and assessing treatment delivery protocols.

The NAA measurements of average concentration of AuNS in PC-3 xenografts demonstrated uptake in tumors and, as expected, AuNS phagocytosis in the mononuclear phagocyte system resulted in substantial accumulation in liver and spleen. While the uptake in the spleen and liver was similar to previous reports, the tumor uptake was about $1/10^{th}$ [36]. The large non-specific uptake necessarily limits what organs this technology may be applied to. As the maximal heating near the surface is dominated by absorption, the average concentration of gold in the tumor can be used to crudely estimate the expected maximum temperature in the tumor tissue based on previous controlled MRTI measurements of temperature changes of the same particles in an agar phantom [39]. In this previous work, approximately 0.167°C per W/cm^2 per μg-Au/g-agar was observed. Using the average 11.24 μg-Au/g-tissue measured here and 4 W/cm^2, gives an expected temperature change of 7.5°C, substantially less than measured here. However, the measured NAA concentration assumes a uniform distribution of AuNS throughout the tissue, which is contradicted by our microscopy observations as well as previous literature on the subject. Bhujwalla et al have reported measurements of vascular volume and permeable volumes as a percentage of overall tumor volume for PC-3 tumors [42]. In fact, the reduced permeability of the PC-3 model in their work may provide a good explanation of the reduced tumor uptake measured in this work. If we revise our estimated maximal heating using their measurement of percent of PC-3 tumor volume that is permeable (36.6%), the estimated temperature rise 20.3°C, which is in fairly reasonable agreement with our measured difference (AuNS – control) of 21.7°C in light of the differences between the *in vivo* and phantom scenarios. Similarly, by using the percent of tumor tissue enhancing on our silver stain image from the peripheral cortex (30% using mean background + 2σ is used as a threshold), we can also refine the estimated concentration of AuNS for that subject. In this case, the estimated maximum temperature rise is 24.8°C versus the 25.8°C measured by MRTI. Again, reasonable agreement is observed via this simple estimation.

CONCLUSIONS

This research has demonstrated that passive uptake of intravenously injected AuNS in PC-3 xenografts transforms permeable tumor vasculature into a potent heating source throughout

the tumor for nanoparticle mediated laser ablation. Ablative temperatures can be reached within minutes at power levels which do not generate significant damage in normal tissue which is in close proximity of the laser compared to laser ablation protocols which do not use nanoparticles. MRTI provides an effective way of monitoring the intratumoral spatiotemporal distribution of temperature in real time. This has implications in the design, monitoring and control of therapy delivery for interstitial laser ablative therapy in cases where it is highly desirable for therapy to better conform to the shape of the tumor than the ellipsoidal heating of the laser fiber. The ability to design and deliver such therapies requires further investigation using larger tumor models and interstitial delivery.

Acknowledgments

The authors would like to acknowledge that this research is supported in part by the National Institutes of Health through MD Anderson's Cancer Center Support Grant CA016672. Additionally, the authors would like to thank Andrei Y. Volgin, PhD for his expertise in developing the PC-3 cell culture techniques for the inoculations performed in this study, Corazon Bucana, PhD and Robert Langley, PhD for their assistance in the design and acquisition of the microscopy data, and Marilene Paquet D.V.M. for her assistance with the histopathology analysis.

REFERENCES

1. Ahmed M, Brace CL, Lee FT Jr. Goldberg SN. Principles of and advances in percutaneous ablation. Radiology. 2011; 258(2):351–69. [PubMed: 21273519]
2. Requarth J. Image-guided palliative care procedures. Surg Clin North Am. 2011; 91(2):367–402. [PubMed: 21419259]
3. Thumar AB, Trabulsi EJ, Lallas CD, Brown DB. Thermal ablation of renal cell carcinoma: triage, treatment, and follow-up. J Vasc Interv Radiol. 2010; 21(8 Suppl):S233–41. [PubMed: 20656233]
4. Pua BB, Thornton RH, Solomon SB. Ablation of pulmonary malignancy: current status. J Vasc Interv Radiol. 2010; 21(8 Suppl):S223–32. [PubMed: 20656232]
5. Sharma R, Wagner JL, Hwang RF. Ablative Therapies of the Breast. Surgical Oncology Clinics of North America. 2011; 20(2):317–339. [PubMed: 21377586]
6. Kurup AN, Callstrom MR. Ablation of skeletal metastases: current status. J Vasc Interv Radiol. 2010; 21(8 Suppl):S242–50. [PubMed: 20656234]
7. Flanders VL, Gervais DA. Ablation of liver metastases: current status. J Vasc Interv Radiol. 2010; 21(8 Suppl):S214–22. [PubMed: 20656231]
8. McWilliams JP, Yamamoto S, Raman SS, Loh CT, Lee EW, Liu DM, Kee ST. Percutaneous ablation of hepatocellular carcinoma: current status. J Vasc Interv Radiol. 2010; 21(8 Suppl):S204–13. [PubMed: 20656230]
9. Colen RR, Jolesz FA. Future potential of MRI-guided focused ultrasound brain surgery. Neuroimaging Clin N Am. 2010; 20(3):355–66. [PubMed: 20708551]
10. Erinjeri JP, Clark TW. Cryoablation: mechanism of action and devices. J Vasc Interv Radiol. 2010; 21(8 Suppl):S187–91. [PubMed: 20656228]
11. Hong K, Georgiades C. Radiofrequency ablation: mechanism of action and devices. J Vasc Interv Radiol. 2010; 21(8 Suppl):S179–86. [PubMed: 20656227]
12. Lubner MG, Brace CL, Hinshaw JL, Lee FT Jr. Microwave tumor ablation: mechanism of action, clinical results, and devices. J Vasc Interv Radiol. 2010; 21(8 Suppl):S192–203. [PubMed: 20656229]
13. Jolesz FA. MRI-guided focused ultrasound surgery. Annu Rev Med. 2009; 60:417–30. [PubMed: 19630579]
14. Pauly KB, Diederich CJ, Rieke V, Bouley D, Chen J, Nau WH, Ross AB, Kinsey AM, Sommer G. Magnetic resonance-guided high-intensity ultrasound ablation of the prostate. Top Magn Reson Imaging. 2006; 17(3):195–207. [PubMed: 17414077]
15. Stafford R, Fuentes D, Elliott AA, Weinberg JS, Ahrar K. Laser-Induced Thermal Therapy for Tumor Ablation. Critical reviews in biomedical engineering. 2010; 38(1):79. [PubMed: 21175405]

16. Rieke V, Butts Pauly K. MR thermometry. J Magn Reson Imaging. 2008; 27(2):376–90. [PubMed: 18219673]

17. McDannold N. Quantitative MRI-based temperature mapping based on the proton resonant frequency shift: review of validation studies. Int J Hyperthermia. 2005; 21(6):533–46. [PubMed: 16147438]

18. Raz O, Haider MA, Davidson SR, Lindner U, Hlasny E, Weersink R, Gertner MR, Kucharczyk W, McCluskey SA, Trachtenberg J. Real-time magnetic resonance imaging-guided focal laser therapy in patients with low-risk prostate cancer. Eur Urol. 2010; 58(1):173–7. [PubMed: 20334965]

19. Carpentier A, McNichols RJ, Stafford RJ, Itzcovitz J, Guichard JP, Reizine D, Delaloge S, Vicaut E, Payen D, Gowda A, et al. Real-time magnetic resonance-guided laser thermal therapy for focal metastatic brain tumors. Neurosurgery. 2008; 63(1 Suppl 1):ONS21–8. discussion ONS28–9. [PubMed: 18728600]

20. Kickhefel A, Rosenberg C, Weiss CR, Rempp H, Roland J, Schick F, Hosten N. Clinical evaluation of MR temperature monitoring of laser induced thermotherapy in human liver using the proton resonance frequency method and predictive models of cell death. Journal of Magnetic Resonance Imaging. 2011; 33(3):704–709. [PubMed: 21563256]

21. Hirsch LR, Gobin AM, Lowery AR, Tam F, Drezek RA, Halas NJ, West JL. Metal nanoshells. Ann Biomed Eng. 2006; 34(1):15–22. [PubMed: 16528617]

22. Krishnan S, Diagaradjane P, Cho SH. Nanoparticle-mediated thermal therapy: evolving strategies for prostate cancer therapy. Int J Hyperthermia. 2010; 26(8):775–89. [PubMed: 20858069]

23. Hirsch LR, Stafford RJ, Bankson JA, Sershen SR, Rivera B, Price RE, Hazle JD, Halas NJ, West JL. Nanoshell-mediated near-infrared thermal therapy of tumors under magnetic resonance guidance. Proc Natl Acad Sci U S A. 2003; 100(23):13549–54. [PubMed: 14597719]

24. Schwartz JA, Shetty AM, Price RE, Stafford RJ, Wang JC, Uthamanthil RK, Pham K, McNichols RJ, Coleman CL, Payne JD. Feasibility study of particle-assisted laser ablation of brain tumors in orthotopic canine model. Cancer Res. 2009; 69(4):1659–67. [PubMed: 19208847]

25. Jain RK, Stylianopoulos T. Delivering nanomedicine to solid tumors. Nat Rev Clin Oncol. 2010; 7(11):653–64. [PubMed: 20838415]

26. Diagaradjane P, Shetty A, Wang JC, Elliott AM, Schwartz J, Shentu S, Park HC, Deorukhkar A, Stafford RJ, Cho SH, et al. Modulation of in vivo tumor radiation response via gold nanoshell-mediated vascular-focused hyperthermia: characterizing an integrated antihypoxic and localized vascular disrupting targeting strategy. Nano Lett. 2008; 8(5):1492–500. [PubMed: 18412402]

27. Oldenburg SJ, Averitt RD, Westcott SL, Halas NJ. Nanoengineering of optical resonances. Chemical Physics Letters. 1998; 288:243–247.

28. Duff DG, Baiker A. A New Hydrosol of Gold Clusters. 1. Formation and Particle Size Variation. Langmuir. 1993; 9:2301–2309.

29. Veronese FM, Pasut G. PEGylation, successful approach to drug delivery. Drug Discov Today. 2005; 10(21):1451–8. [PubMed: 16243265]

30. Hindman JC. Proton resonance shift of water in the gas and liquid states. Journal of Chemical Physics. 1966; 44(12):4582–4592.

31. Kuroda K. Non-invasive MR thermography using the water proton chemical shift. Int J Hyperthermia. 2005; 21(6):547–60. [PubMed: 16147439]

32. Chung AH, Hynynen K, Colucci V, Oshio K, Cline HE, Jolesz FA. Optimization of spoiled gradient-echo phase imaging for in vivo localization of a focused ultrasound beam. Magn Reson Med. 1996; 36(5):745–52. [PubMed: 8916025]

33. Ishihara Y, Calderon A, Watanabe H, Okamoto K, Suzuki Y, Kuroda K. A precise and fast temperature mapping using water proton chemical shift. Magn Reson Med. 1995; 34(6):814–23. [PubMed: 8598808]

34. Peters RD, Hinks RS, Henkelman RM. Ex vivo tissue-type independence in proton-resonance frequency shift MR thermometry. Magn Reson Med. 1998; 40(3):454–9. [PubMed: 9727949]

35. De Poorter J. Noninvasive MRI thermometry with the proton resonance frequency method: study of susceptibility effects. Magn Reson Med. 1995; 34(3):359–67. [PubMed: 7500875]

36. James WD, Hirsch LR, West JL, O'Neal PD, Payne JD. Application of INAA to the build-up and clearance of gold nanoshells in clinical studies in mice. Journal of Radioanalytical and Nuclear Chemistry. 2007; 271(2):455–459.

37. Coad JE, Kosari K, Humar A, Sielaff TD. Radiofrequency ablation causes `thermal fixation' of hepatocellular carcinoma: a post-liver transplant histopathologic study. Clin Transplant. 2003; 17(4):377–84. [PubMed: 12868996]

38. van Gemert MJ, Lucassen GW, Welch AJ. Time constants in thermal laser medicine: II. Distributions of time constants and thermal relaxation of tissue. Phys Med Biol. 1996; 41(8):1381–99. [PubMed: 8858726]

39. Elliott AM, Schwartz J, Wang J, Shetty AM, Bourgoyne C, O'Neal DP, Hazle JD, Stafford RJ. Quantitative comparison of delta P1 versus optical diffusion approximations for modeling near-infrared gold nanoshell heating. Med Phys. 2009; 36(4):1351–8. [PubMed: 19472642]

40. Stern JM, Stanfield J, Kabbani W, Hsieh JT, Cadeddu JA. Selective prostate cancer thermal ablation with laser activated gold nanoshells. J Urol. 2008; 179(2):748–53. [PubMed: 18082199]

41. Park J, Estrada A, Schwartz JA, Diagaradjane P, Krishnan S, Dunn AK, Tunnell JW. Intra-organ Biodistribution of Gold Nanoparticles Using Intrinsic Two-photon Induced Photoluminescence. Lasers Surg Med. 2010; 42(7):630–639. [PubMed: 21399728]

42. Bhujwalla ZM, Artemov D, Natarajan K, Ackerstaff E, Solaiyappan M. Vascular differences detected by MRI for metastatic versus nonmetastatic breast and prostate cancer xenografts. Neoplasia. 2001; 3(2):143–53. [PubMed: 11420750]

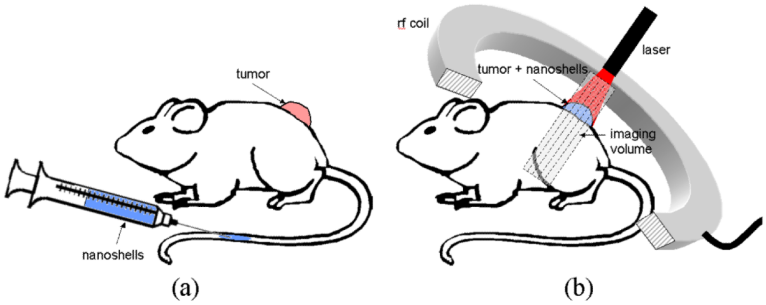

Figure 1. MRTI Imaging of AuNS Mediated Heating Schematic

Tumors were grown on the backs of SCID mice. 24-hours prior to treatment, PEGylated AuNS suspended in phosphate buffered saline were injected via tail vein and allowed to circulate. On treatment day, mice were anesthetized and tumors illuminated with a laser under real-time magnetic resonance temperature image monitoring.

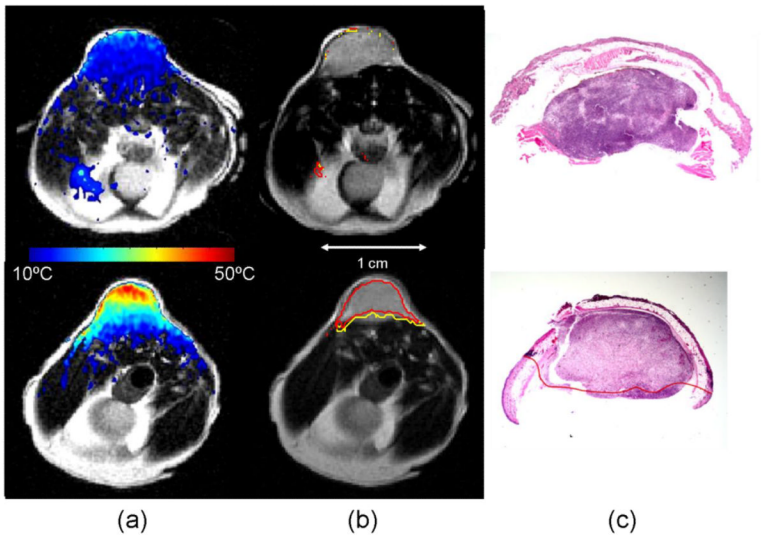

Figure 2. AuNS Mediated Heating

Calculated maximum change in temperature (color) is mapped onto T2-W anatomical images of the mouse xenografts (column a). Relatively low heating is observed in the control (top) versus the highly tumor specific heating observed in the +AuNS tumor (bottom). The cumulative minutes at 43°C (t_{43}) thermal dose was estimated from the temperature history (column b) and the 240 min (red) and 90 min (yellow) isotherms are shown to demonstrate the rapid dose gradient with depth in tissue. H&E staining of tissue post-treatment (column c) demonstrates the correlation between observed damage (red) in the +AuNS versus the expectations from MRTI (columns a&b)..

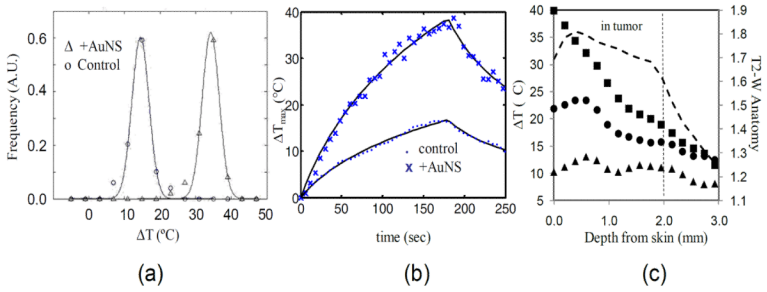

Figure 3. MRTI Evaluation of Spatiotemporal Temperature Changes

Gaussian distributions were fit (solid lines) to binned histogram data of temperature changes in a control (◯) and +AuNS (Δ) tumors (a) to further demonstrate the clear differences (19.2°C) in temperature distribution observed between a control (ΔT_{max} = 17.6°C) and +AuNS (ΔT_{max} = 36.8°C) tumors. Temporal temperature history (b) demonstrated the rapid heating of +AuNS (X) versus a control (·) over the 180 sec exposure at 4W/cm^2 and the shape of the curve at maximum temperature correlated well with theory (solid lines). Spatial profiles of the temperature (c) taken at 45sec (▲), 90 sec (•) and 180 sec (■) for a +AuNS tumor help demonstrate that the primary source of heating came from just distal to the skin surface within the cortex of the tumor when correlated with the region of tumor on T2-W MRI (----).

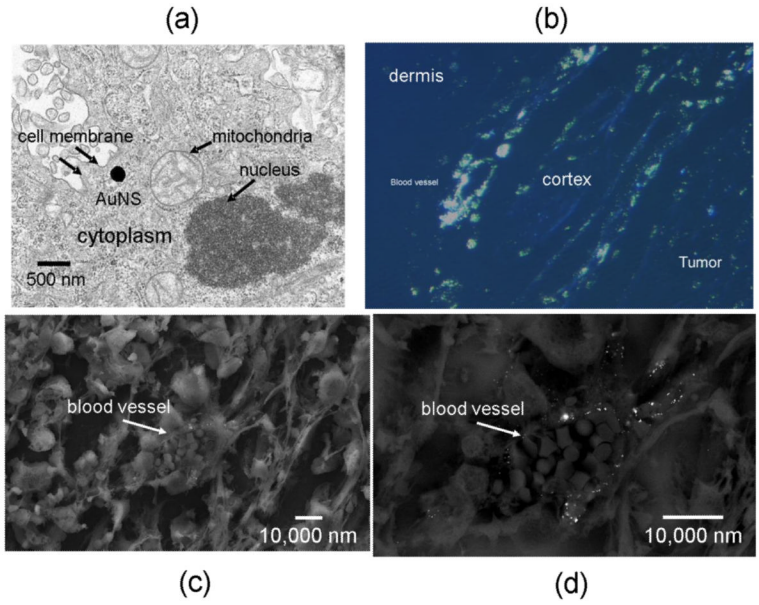

Figure 4. Microscopy of AuNS in PC-3 xenografts

TEM illustrates the size of the AuNS (140–150 nm) in relation to cellular organelles (a). Silver staining of the AuNS on polarized fluorescent microscopy (b) corroborated the observation that uptake near blood vessels which were most plentiful in the peripheral tumor cortex. SEM of individual vessels (c) further implied that the passively extravasated AuNS tended to cluster in the perivascular space (d).